

# Nanoscale subcellular architecture revealed by multicolor three-dimensional salvaged fluorescence imaging

Yongdeng Zhang<sup>1,11</sup>, Lena K. Schroeder<sup>1,11</sup>, Mark D. Lessard<sup>1</sup>, Phylicia Kidd<sup>1</sup>, Jeeyun Chung<sup>1,2,3</sup>, Yuanbin Song<sup>4</sup>, Lorena Benedetti<sup>1,2,3</sup>, Yiming Li<sup>5</sup>, Jonas Ries<sup>5</sup>, Jonathan B. Grimm<sup>6</sup>, Luke D. Lavis<sup>6</sup>, Pietro De Camilli<sup>1,2,3,7</sup>, James E. Rothman<sup>1,8</sup>, David Baddeley<sup>1,8,9</sup> and Joerg Bewersdorf<sup>1,7,8,10\*</sup>

**Combining the molecular specificity of fluorescent probes with three-dimensional imaging at nanoscale resolution is critical for investigating the spatial organization and interactions of cellular organelles and protein complexes. We present a 4Pi single-molecule switching super-resolution microscope that enables ratiometric multicolor imaging of mammalian cells at 5–10-nm localization precision in three dimensions using ‘salvaged fluorescence’. Imaging two or three fluorophores simultaneously, we show fluorescence images that resolve the highly convoluted Golgi apparatus and the close contacts between the endoplasmic reticulum and the plasma membrane, structures that have traditionally been the imaging realm of electron microscopy. The salvaged fluorescence approach is equally applicable in most single-objective microscopes.**

While ‘form follows function’ is a well-established principle in architecture, resolving subcellular morphology to understand basic operating principles of a cell has been hampered by a lack of suitable imaging tools. Revealing the intricate inner workings of cells requires visualizing the interactions between proteins and organelles with molecular specificity at nanoscale resolution in three dimensions. The diffraction-limited resolution of conventional light microscopy (about 250 nm) stands in stark contrast to the structural dimensions of many organelles and complexes, such as the thickness of Golgi cisternae (about 50 nm each)<sup>1</sup> and the diameter of tubules of the endoplasmic reticulum (ER) (about 80–100 nm)<sup>2</sup>. Electron microscopy, while providing sufficient resolution with ease, lacks many of the tools that offer molecular specificity in fluorescence light microscopy. Recently developed fluorescence super-resolution techniques have overcome the diffraction barrier and achieved impressive resolutions<sup>3,4</sup>. However, the ultimate goal—simultaneously resolving multiple targets of interest; for example, the spatial relationship between two proteins in the context of a related organelle in three dimensions—is still very challenging and has constrained the impact of super-resolution microscopy in cell biology.

To address this challenge, we set out to develop a super-resolution instrument that can obtain high-quality images in three color channels. We sought to achieve better than 10-nm localization precision in three dimensions, high molecular detection efficiency and negligible channel shift and cross-talk. Two previous inventions in the super-resolution field form the foundation of our

development. (1) Interferometric detection of fluorescence from individual emitters by two opposing objectives in a ‘4Pi’ geometry with single-molecule switching (4Pi-SMS) has demonstrated an improvement in axial localization precision matching or surpassing the lateral values<sup>5–8</sup>. This imaging modality has also been shown to obtain multicolor data of biological structures close to the coverslip by sequential imaging<sup>8–10</sup>. However, multicolor imaging over the whole depth of a cell remains difficult as the channel registration becomes challenging when imaging deep in the samples due to the depth-dependent distortions<sup>11,12</sup> and the refractive index heterogeneities within the specimens<sup>13</sup> (Supplementary Note 1). (2) Ratiometric color assignment can determine molecular identities based on the spectral information extracted from spectrally similar fluorescent emitters that are excited by one laser and imaged simultaneously<sup>14–19</sup>. This approach allows for the use of multiple far-red dyes, many of which have been shown to outperform the majority of dyes in other wavelength ranges with regards to the number of detected photons per switching event, on-off duty cycle and number of switching cycles<sup>18,20</sup>, and reduces the chromatic aberrations. Ratiometric color assignment has struggled so far, however, with obtaining high assignment efficiency without rejecting or falsely assigning large fractions of molecules, and doing so without substantially compromising localization precision. Combining interferometric 4Pi-SMS imaging with a refined ratiometric detection scheme, which takes advantage of ‘salvaged fluorescence’ (SF), we show in this work imaging of mammalian cells at 5–10-nm localization precision in three colors simultaneously.

<sup>1</sup>Department of Cell Biology, Yale School of Medicine, New Haven, CT, USA. <sup>2</sup>Department of Neuroscience, Yale School of Medicine, New Haven, CT, USA. <sup>3</sup>Howard Hughes Medical Institute, Yale School of Medicine, New Haven, CT, USA. <sup>4</sup>Section of Hematology, Department of Internal Medicine, Yale School of Medicine, New Haven, CT, USA. <sup>5</sup>Cell Biology and Biophysics Unit, European Molecular Biology Laboratory, Heidelberg, Germany. <sup>6</sup>Janelia Research Campus, Howard Hughes Medical Institute, Ashburn, VA, USA. <sup>7</sup>Kavli Institute for Neuroscience, Yale School of Medicine, New Haven, CT, USA. <sup>8</sup>Nanobiology Institute, Yale University, West Haven, CT, USA. <sup>9</sup>Auckland Bioengineering Institute, University of Auckland, Auckland, New Zealand. <sup>10</sup>Department of Biomedical Engineering, Yale University, New Haven, CT, USA. <sup>11</sup>These authors contributed equally: Yongdeng Zhang, Lena K. Schroeder. \*e-mail: [joerg.bewersdorf@yale.edu](mailto:joerg.bewersdorf@yale.edu)

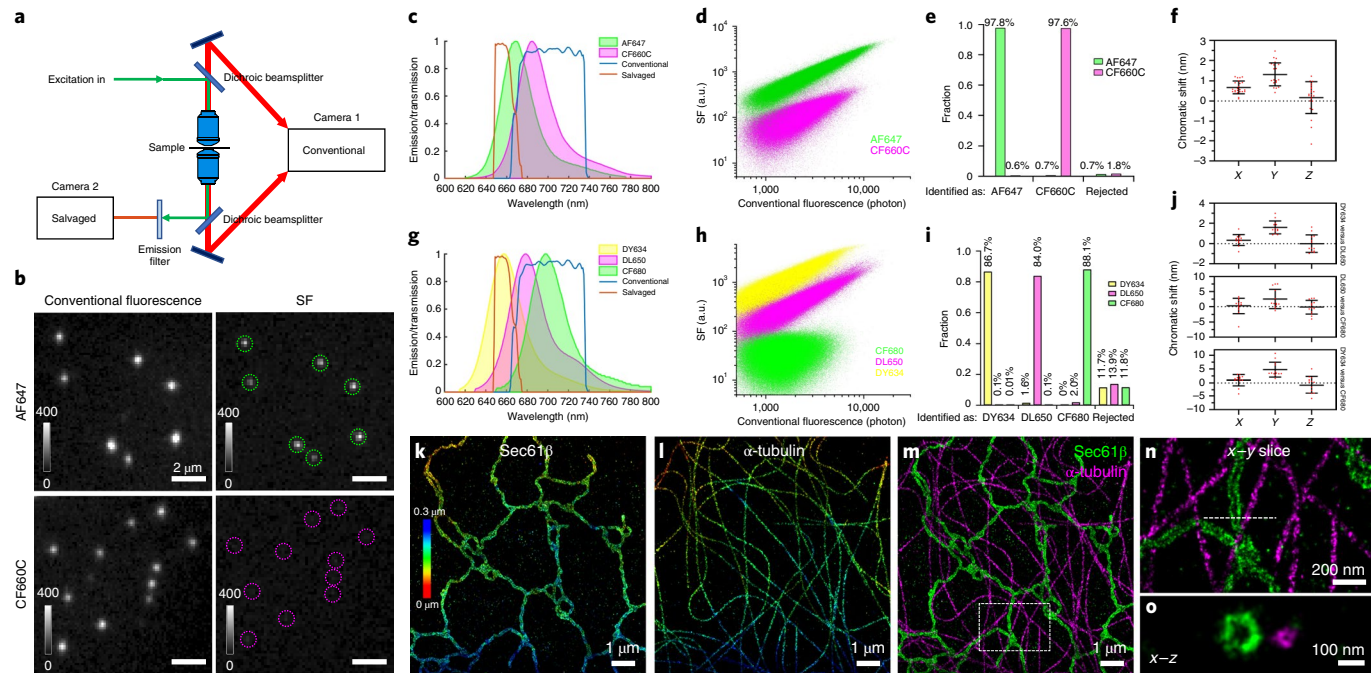


**Fig. 1 | Characterization of multicolor 4Pi-SMS imaging using SF.** **a**, Schematic of the multicolor 4Pi-SMS microscope. Camera 1 captures conventional fluorescence. Camera 2 captures SF. **b**, Conventional fluorescence and SF images of single molecules of AF647 and CF660C (Supplementary Video 1). Dashed circles indicate the positions of single molecules observed in the conventional fluorescence channel. **c**, Emission spectra of AF647 and CF660C and transmission profiles for conventional fluorescence and SF. **d**, Scatter plot of SF versus conventional fluorescence intensities of localized dye molecules in two single-color microtubule samples (shown in Supplementary Fig. 4) on a logarithmic scale. **e**, Cross-talk and rejected fraction for the two dyes. **f**, Chromatic shift between AF647 and CF660C in each dimension, determined from 23 images (each  $20 \times 20 \mu\text{m}^2$ ). **g**, Emission spectra of DY634, DL650 and CF680 and the transmission profiles for conventional fluorescence and SF. **h**, Scatter plot of SF versus conventional fluorescence intensities of localized dye molecules in three single-color microtubule samples (shown in Supplementary Fig. 5) on a logarithmic scale. **i**, Cross-talk and rejected fraction for the three dyes. **j**, Chromatic shift between each dye pair, determined from 13 images (each  $20 \times 20 \mu\text{m}^2$ ). **k, l**, Two-color images of ER membrane (**k**) and microtubules (**l**) in a COS-7 cell. Color bar denotes depth. **m**, Merged image of the two labels shown in **k** and **l**. **n**, A 50-nm-thick x-y slice of the boxed region in **m**. **o**, A 20-nm-thick x-z cross-section along the dashed line in **n**. Data are presented as mean  $\pm$  s.d. in **f** and **j**. Representative images of two (**b**) or five (**k-o**) independent experiments are shown. Spectra shown in **c** and **g** were obtained from the respective manufacturers' websites. a.u., arbitrary units derived from fitted Gaussian-weighted intensity.

## Results

**Implementation of multicolor 4Pi-SMS using SF.** Ratiometric single-molecule imaging assigns molecular identity by comparing the single-molecule emitter signal levels detected in two or more spectral windows<sup>14–19</sup>. If emission spectra are known and the signal-to-noise ratio is sufficiently high, two spectral windows are sufficient to distinguish more than two, in theory an arbitrarily large number of, different fluorescent probes<sup>14</sup>. The classical implementation of ratiometric single-molecule imaging inserts a dichroic beamsplitter into the fluorescence beam path to create these two spectral detection windows. We realized that the main dichroic beamsplitter used in most fluorescent microscopes to separate the illumination from the fluorescence light already represents two spectral windows: the main transmitted, longer-wavelength component (conventional fluorescence) and a small but non-negligible reflected fraction (Fig. 1a and Supplementary Fig. 1). Salvaging this reflected fluorescence provides previously lost spectral information that can be used to assign the molecular identity of an emitter. This approach takes advantage of the fact that spectral assignment and spatial localization precision utilize the fluorescent signal very differently. The former takes advantage of differences between probe spectra, which, given the steep rising edge of the emission spectra, are detected very clearly in the reflected spectral window. This suggests that the SF window can be quite narrow. The latter depends on the total photon number which, with a narrow SF window, is mostly collected in the conventional fluorescence channel. Molecules can then be localized

based on this channel alone, avoiding the need for accurate registration and chromatic corrections necessary in classical ratiometric imaging which combines the signal of both channels. Simulations showed that with a transition edge between windows in the 660–670-nm range, dyes excitable at 642 nm and suitable for single-molecule switching microscopy<sup>18</sup> can be well separated (cross-talk 1–2%, rejection fractions <1% to 10%) with only minor compromises (~1 nm) in localization precision (Supplementary Fig. 2).

We implemented the SF approach in a 4Pi-SMS instrument (Fig. 1a and Supplementary Fig. 1) and tested it with five previously reported<sup>18</sup> far-red dyes (Alexa Fluor 647 (AF647), CF660C, Dyomics 634 (DY634), Dylight 650 (DL650), CF680) for two- and three-color imaging (Fig. 1 and Supplementary Fig. 3). These dyes can be combined into pairs or triplets with about 20-nm spectral emission peak differences, making them good candidates for our SF approach, and can all be excited at 642 nm and efficiently detected in one spectral window (see Methods). For two-color imaging with AF647 and CF660C (Fig. 1b–f and Supplementary Video 1), we achieved a localization precision (~7 nm in xy, ~5 nm in z) that is comparable to the previously reported one-color 4Pi-SMS imaging<sup>8</sup> and Fourier shell correlation (FSC)<sup>21</sup> values of 25 and 22 nm, respectively (Supplementary Fig. 4a–f). Consistent with these high localization precision values, the microscope can resolve the hollow center of labeled ER tubules (~100 nm in diameter) and microtubules (~45 nm in diameter: 26-nm actual diameter plus ~10-nm displacement on either side caused by using

antibodies) (Fig. 1k–o). The distinct ratios of SF to conventional fluorescence between the two dyes yielded a cross-talk of <1% (Fig. 1d,e and Supplementary Fig. 4g,h). The average chromatic shifts between the two channels were determined to be less than 2 nm in all directions without applying any chromatic corrections (Fig. 1f and Supplementary Fig. 4i–k).

Using DY634, DL650 and CF680 for three-color imaging (Fig. 1g–j), we resolved the tubular structure of immunolabeled microtubules in all three color channels (FSC values, DY634, 32 nm; DL650, 25 nm; CF680, 28 nm; Supplementary Fig. 5a–i), and achieved  $\leq 2\%$  cross-talk between each dye pair (Fig. 1i and Supplementary Fig. 5j,k). The average chromatic shifts between the three dyes were determined to be mostly in the 1–3-nm range with the biggest value being <5 nm for the dyes with the farthest-shifted spectra (Fig. 1j and Supplementary Fig. 5l,m).

**Multicolor 4Pi-SMS imaging of ER, mitochondria and synaptosomal complexes.** We further tested our SF approach by imaging spatially close cellular structures with known geometries (Fig. 2). The luminal and membrane markers of ER were resolved with no apparent chromatic aberrations despite the small diameter (Fig. 2a–e, Supplementary Fig. 6a–c and Supplementary Video 2). The high three-dimensional (3D) resolution revealed the substantial differences between two immunolabeling approaches: the apparent ER tubule diameter is about 20 nm smaller when labeled with a nanobody compared with conventional primary and secondary antibodies (Supplementary Fig. 6d–i), showing that using primary and secondary antibodies increased the displacement between labeled target and dyes by ~10 nm, which is consistent with previous reports<sup>22,23</sup>. Mitochondrial double-stranded DNA (dsDNA) was positioned within and clearly isolated from the outer mitochondrial membrane at various depths (Fig. 2f–i, Supplementary Fig. 7a–c and Supplementary Video 3). In contrast, two outer mitochondrial membrane proteins were in close proximity throughout the volume of the sample (Supplementary Fig. 7d–k), confirming that our method results in alignment errors of less than 4 nm without applying any chromatic corrections, even in thicker volumes.

To demonstrate the power of the SF approach in thicker cells, we imaged the synaptosomal complex in intact mouse spermatocytes (Fig. 2j–q, Supplementary Fig. 8 and Supplementary Video 4). Our method revealed the twisted helical structure of two synaptosomal scaffold proteins, SYCP1 and SYCP3, throughout the 10-μm-thick volume (Fig. 2j–o and Supplementary Fig. 8a–d). Furthermore, imagining N- and C-terminally labeled SYCP1 confirmed that the C terminus is oriented towards the SYCP3 tracks while the N terminus extends into the central region<sup>24</sup> (Fig. 2j,m). Imaging these two proteins alongside Lamin B showed the ends of the synaptosomal complexes connecting to the nuclear lamina (Supplementary Fig. 8e,f), confirming previous results<sup>25</sup>. The ends of fully assembled (Fig. 2p) as well as partially assembled synaptosomal complexes (Fig. 2q) are closely associated with the lamina.

**Multicolor 4Pi-SMS imaging of Golgi apparatus.** The minimal cross-talk and negligible chromatic aberrations make the SF approach a powerful tool for cell biology. To test how well it can reveal the location of proteins in complex 3D morphologies that are otherwise only accessible through EM, we imaged two challenging structures that are of central importance to cell biology: the Golgi apparatus and contact sites between the ER and the plasma membrane (PM).

We imaged the immunolabeled Golgi apparatus in HeLa cells in three colors (Fig. 3a–e, Supplementary Fig. 9 and Supplementary Video 5). The *cis*, medial and *trans* regions appeared as distinct structures stacked parallel to each other in cross-sections through the imaged Golgi apparatus (Fig. 3f,g). While the *cis*-medial-*trans* stacking was maintained throughout the Golgi, some stacks flipped

their orientation within a few hundred nanometers (Fig. 3f, compare dashed line and cyan arrow). The high 3D resolution enabled us to characterize the distance between *cis*, medial and *trans* cisternae despite the convoluted morphology of the Golgi apparatus (Fig. 3h,i). The *trans*-localized p230 and *cis*-localized GRASP65 labels showed a peak-to-peak distance of on average 187 nm, ranging from 141 nm (10th percentile) to 236 nm (90th percentile). This broad distribution of the peak-to-peak distances appeared to consist of two populations, which suggests that we observed Golgi stacks with different numbers of cisternae. The medial-localized ManII was on average 85 nm (10th percentile: 50 nm; 90th percentile: 116 nm) apart from GRASP65. In contrast, GRASP65 and the also *cis*-localized GM130 showed an average separation not significantly different from zero ( $P=0.62$ ) (Supplementary Fig. 10), confirming previous biochemical data<sup>26</sup>. It has been previously reported that each Golgi cisterna is about 50-nm thick<sup>1</sup>. Side profile measurements of our data showed that both p230 and GM130 stainings had an average thickness of 77 nm and 86 nm, respectively (Fig. 3h,j). This is an overestimate as we averaged across 1-μm subregions and did not account for the fact that the cisternae are not perfectly flat over these regions. Considering the ~10-nm displacement added by antibody labeling on each side of a cisterna (Supplementary Fig. 6i), these data suggests that p230 and GM130 are enriched in one cisterna only, as expected. Our GRASP65 staining showed a similar thickness to p230 and GM130 (Fig. 3j), indicating that our GRASP65 labeling is concentrated in one cisterna. In contrast, ManII-GFP appeared at an average thickness of 127 nm, implying that it is distributed over multiple cisternae (Fig. 3j).

**Multicolor 4Pi-SMS imaging of ER-PM contact sites.** Unlike the perinuclear Golgi, the ER spreads and branches throughout the volume of mammalian cells making contacts with most organelles, including the PM. To gain insight into fine details of ER-PM contacts, where the intermembrane distance is typically within the 15–25-nm range<sup>27</sup>, we imaged the PM (labeled with WGA) and ER membranes in COS-7 cells (Fig. 4 and Supplementary Video 6). At the periphery of the cells, ER tubules are generally clearly separated by tens of nanometers from the top and bottom PM (Fig. 4a). On overexpression of an ER protein, ORP5, which functions as a tether at ER-PM contact sites, however, a large fraction of the peripheral ER became closely apposed to the PM to form large, patch-like contacts<sup>28</sup> (Fig. 4b, cyan arrow). Likewise, overexpression of another ER-PM contact site protein, E-Syt2 (ref. <sup>29</sup>), also expanded appositions of ER with the PM, although, in this case, the ER retained a tubular shape at such appositions (Supplementary Fig. 11a). This was consistent with E-Syt2 being anchored to the ER membrane by an N-terminal hairpin domain that may sense/induce high-curvature membranes<sup>29</sup>, while ORP5 is anchored to the ER by a single C-terminal transmembrane region<sup>28</sup>. To visualize the contact site proteins directly, we imaged ORP5 or E-Syt2 together with the PM marker (Fig. 4c–f and Supplementary Fig. 11b–f). In agreement with the results shown above, ORP5 appeared as patches (Supplementary Fig. 11b), while E-Syt2 mostly appeared as tubule-like structures (Supplementary Fig. 11c) and occasionally as small patches (Supplementary Fig. 11d). Two-color imaging further confirmed that the observed ORP5 and E-Syt2 structures corresponded to ER elements (Supplementary Fig. 12a–f). The intensity profile of each cross-section showed a small separation between ORP5 or E-Syt2 and the PM (Fig. 4d,f and Supplementary Fig. 11f, blue arrow). Quantification showed distances of the PM signal peak to the ORP5 and E-Syt2 signal peaks of 15–20 nm (Fig. 4g), respectively, consistent with E-Syt1 and E-Syt3 values derived from electron microscopy images<sup>27</sup> and demonstrating the power of SF in resolving ultrastructural details. While it is difficult to visualize specific contact site proteins in EM, our approach allows imaging of the ER membrane, contact site proteins and the PM at the

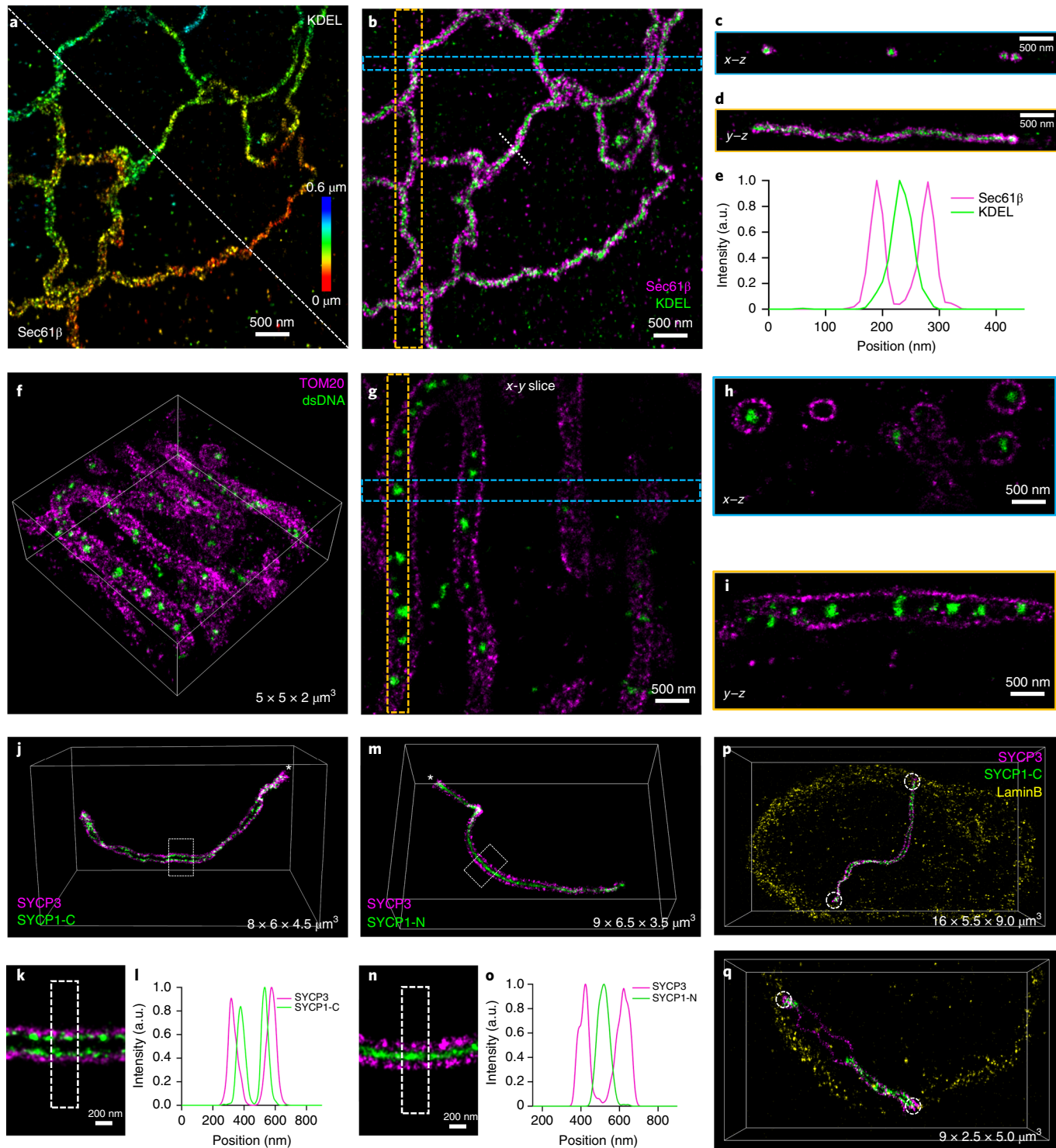


**Fig. 2 | Multicolor 4Pi-SMS images of ER, mitochondria and synaptonemal complexes.** **a**, Two-color image of ER membrane and lumen in a COS-7 cell (Supplementary Video 2). The lower-left and upper-right corners show the Sec61 $\beta$  labeling and KDEL labeling, respectively. Color bar denotes depth. **b**, Merged image of the two labels shown in **a**. **c**, The x-z view of the blue dashed box (200 nm wide) in **b**. **d**, The y-z view of the orange dashed box (400 nm wide) in **b**. **e**, Intensity profile along the white dashed line in **b**. **f**, Two-color image of outer mitochondrial membrane and mitochondrial dsDNA in a HeLa cell (Supplementary Video 3). **g**, A 200-nm-thick x-y slice of the image in **f**. **h**, The x-z view of the blue dashed box (300 nm wide) in **g**. **i**, The y-z view of the orange dashed box (300 nm wide) in **g**. **j**, Computationally isolated two-color image of SYCP3 and SYCP1-C in a synaptonemal complex (Supplementary Fig. 8a,b and Supplementary Video 4, part I). **k**, Magnified image of the boxed region in **j**. **l**, Intensity profile along the dashed boxed region in **k**. **m**, Computationally isolated two-color image of SYCP3 and SYCP1-N in a synaptonemal complex (Supplementary Fig. 8c,d and Supplementary Video 4, part II). **n**, Magnified image of the boxed region in **m**. **o**, Intensity profile along the dashed boxed region in **n**. **p,q**, Three-color images of SYCP3 and SYCP1-C on two computationally isolated, fully (**p**) and partially (**q**) assembled synaptonemal complexes next to Lamin B (Supplementary Fig. 8e,f and Supplementary Video 4, part III). White dashed circles indicate where synaptonemal complexes contact the nuclear lamina. Representative images of one (**a-d**), four (**f-i,p,q**), five (**j** and **k**) or two (**m** and **n**) independent experiments are shown.

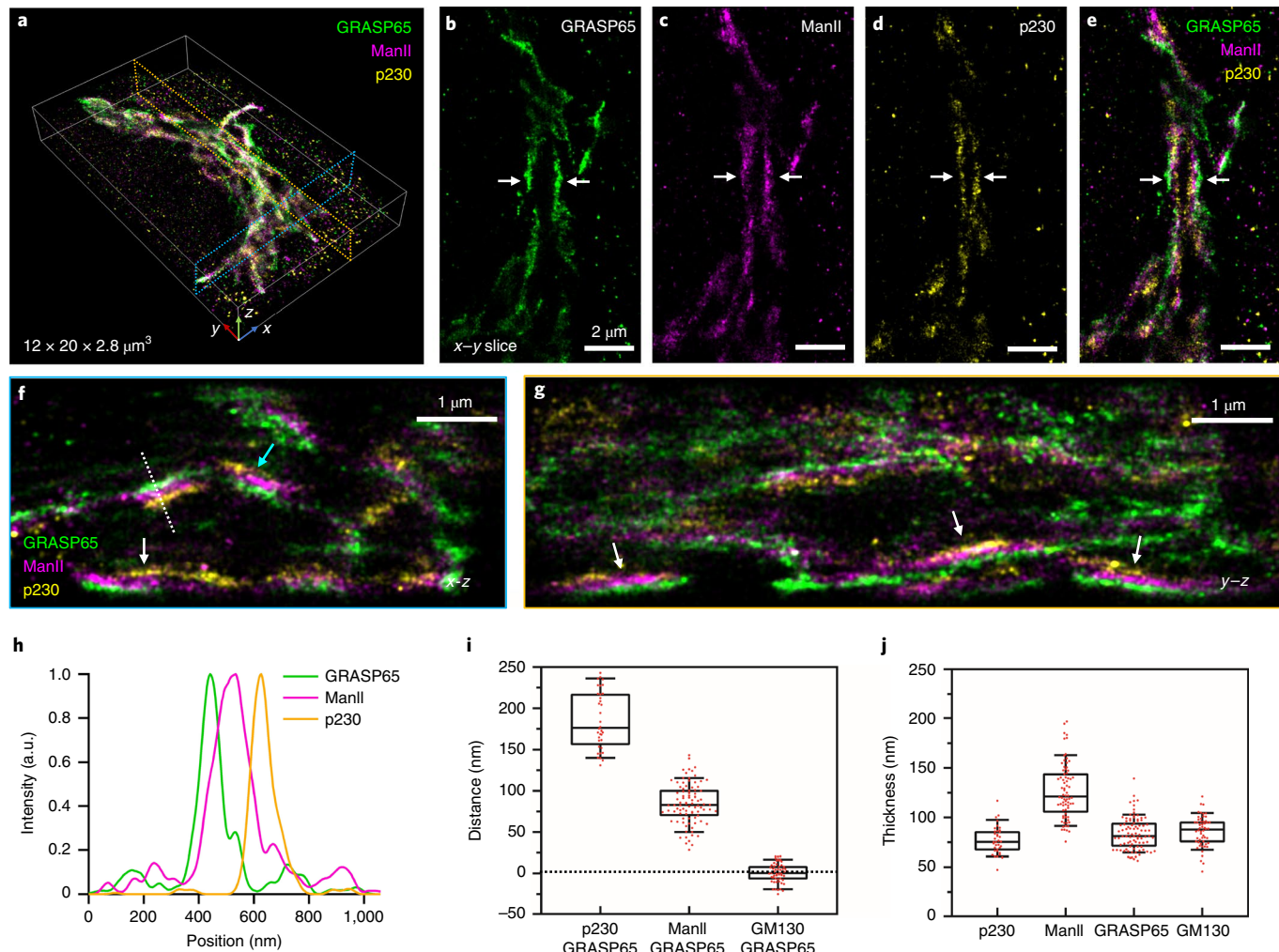


**Fig. 3 | Complex stacked architecture of the Golgi apparatus.** **a**, 3D overlay image of *cis* (GRASP65), medial (ManII) and *trans* (p230) Golgi proteins in a HeLa cell (Supplementary Fig. 9 and Supplementary Video 5, part I). **b–d**, A 500-nm-thick x-y slice of GRASP65 (**b**), ManII (**c**) or p230 (**d**) from the data shown in **a**. **e**, Merged image of the three labels shown in **b–d**. **f**, A 1-μm-thick x-z cross-section centered at the blue dashed region in **a**. **g**, A 1-μm-thick y-z cross-section centered at the orange dashed region in **a**. **h**, Intensity profile along the dashed line in **f**. **i**, Distance between the peak intensities of each pair of Golgi proteins (p230-GRASP65,  $n=36$  from 9 cells; ManII-GRASP65,  $n=90$  from 18 cells; GM130-GRASP65,  $n=54$  from 9 cells). **j**, Thickness of Golgi regions, measured as the FWHM of the intensity profile (p230,  $n=36$  from 9 cells; ManII,  $n=76$  from 18 cells; GRASP65,  $n=90$  from 18 cells; GM130,  $n=54$  from 9 cells). Arrows denote where the *cis*-medial-*trans* stack is visible (**b–g**). Median and interquartile range are shown, with whiskers drawn down to the 10th percentile and up to the 90th percentile (**i** and **j**). Representative images of three independent experiments are shown (**a–g**).

same time. Three-color imaging of ER-PM contact sites showed both contact site proteins as expected at the interface between ER membranes and the PM: ORP5 at patch-like contacts (Fig. 4*h,j* and Supplementary Fig. 12*g*) and E-Syt2 at tubular contacts (Fig. 4*j,k* and Supplementary Fig. 12*h*). In addition, both ORP5 and E-Syt2 localized to the ER membrane facing the PM but not the other side (Fig. 4*h–k* and Supplementary Video 7).

## Discussion

The development of high-quality multicolor imaging at tens-of-nanometers resolution in three dimensions provides a tool to the cell biologist that combines the strength of specific labeling of fluorescence microscopy in the context of interaction partners and cellular landmarks with a level of detail that traditionally had been the realm of electron microscopy.

As we routinely achieve better than 10-nm localization precision, other factors, such as localization density, drift, chromatic aberrations and localization accuracy, become more important<sup>3</sup>. As shown above, chromatic aberrations using our SF approach are

below 5 nm, typically in the 1–3-nm range. Using redundant cross-correlation-based drift correction, residual drift is reduced to below 5 nm (refs. <sup>30,31</sup>). These low values combined with high localization densities allow us to achieve excellent 22–32-nm FSC values in our microtubule data (Supplementary Figs. 4 and 5).

The localization accuracy (representing the systematic offset of the determined positions from the true positions of target proteins) suffers from the size of the label. In most of the imaging shown in this work, we used antibody labeling (primary + secondary) which creates an average displacement of ~10 nm from the targets. Using overexpressed green fluorescent protein (GFP) labeled with anti-GFP nanobody reduces this displacement to 2–6 nm (4-nm size of GFP ± 2-nm size of nanobody) and results in smaller diameters of the ER tubules (Supplementary Fig. 6*i*). To further improve the localization accuracy, genetically encoded self-labeling tags (HaloTag<sup>32</sup> and SNAP-tag<sup>33</sup>) or click-chemistry<sup>34</sup> can be used.

It is important to note that our SF approach with minor optical modifications can also be implemented in single-objective systems (Supplementary Fig. 13*a,b*), where chromatic focal shifts can be

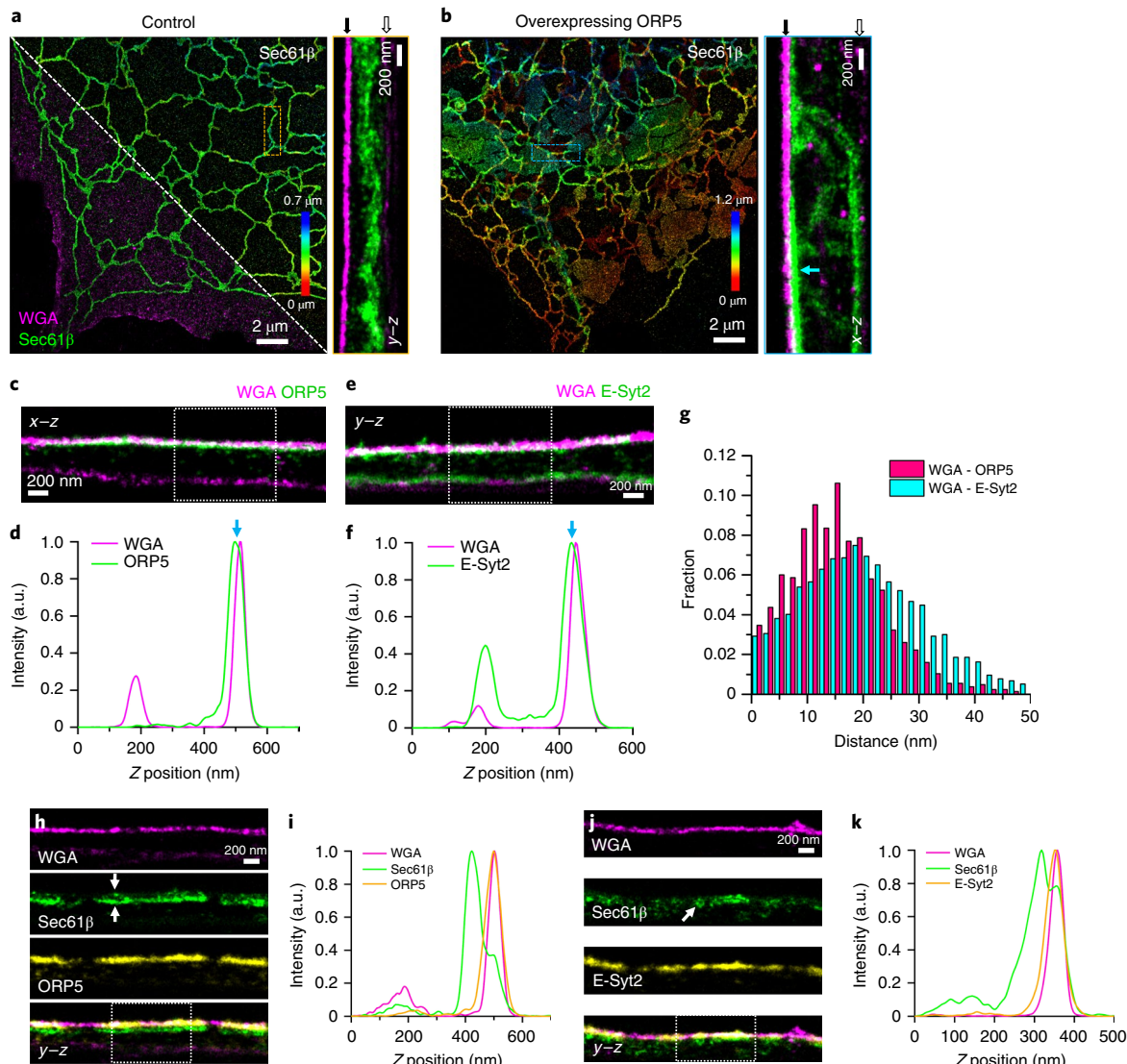


**Fig. 4 | The 3D architecture of ER-PM contact sites.** **a**, Two-color image of ER (Sec61 $\beta$ ) and PM (WGA) in a COS-7 cell (Supplementary Video 6, part I). Top-right half shows the ER, where color bar denotes depth. Bottom left half overlays ER and PM. Right panel shows magnified y-z view of boxed region. **b**, Two-color image of ER and PM in a cell overexpressing mCherry-ORP5 (Supplementary Video 6, part II). Right panel shows magnified x-z view of boxed region. Solid and outlined arrows in **a** and **b** point to the top and bottom PM, respectively. **c**, Two-color ORP5 and PM x-z view (overview shown in Supplementary Fig. 11b). **d**, Axial intensity profile across the dashed box in **c**. **e**, Two-color E-Syt2 and PM y-z view (overview shown in Supplementary Fig. 11c). **f**, Axial intensity profile across the dashed box in **e**. Blue arrows in **d** and **f** indicate the distance between PM and contact site proteins. **g**, Histograms of the distance between PM and contact site proteins (from >2,800 subregions of  $100 \times 100\text{-nm}^2$  size,  $n=4$  cells per condition) (see Methods). **h**, Three-color ER, ORP5 and PM y-z view (overview shown in Supplementary Fig. 12g and Supplementary Video 7, part I). White arrows indicate the top and bottom membranes of the ER. **i**, Axial intensity profile across the dashed box in **h**. **j**, Three-color ER, E-Syt2 and PM y-z view (overview shown in Supplementary Fig. 12h and Supplementary Video 7, part II). White arrow points to an ER tubule. **k**, Axial intensity profile across the dashed box in **j**. Representative images of four (**a**), three (**b** and **c**) or two (**e**, **h** and **j**) independent experiments are shown.

even stronger than in the 4Pi configuration. To show the feasibility, we blocked the top emission beam path in our 4Pi-SMS microscope to mimic the detection of a single-objective system (Supplementary Fig. 13c). We obtained two-color images with excellent quality in both two dimensions and three dimensions with astigmatism (Supplementary Fig. 13d–j). Additionally, the concept can be adopted in many multicolor imaging scenarios, including other single-molecule imaging techniques and single-particle tracking, or in systems optimized for large field-of-view imaging with uniform illumination<sup>35,36</sup>.

Similar to classical ratiometric approaches, the ability of our SF approach to image multiple dyes simultaneously, in theory, can

reduce the acquisition time. However, in practice, the acquisition speed is often limited by the need to avoid the spatial overlap of blinking molecules which puts a constraint on the maximum number of blinking molecules per frame. Given that multicolor imaging at super-resolution is usually most helpful to reveal the relationship between multiple molecular species in close proximity, molecules from different stainings, which in ratiometric imaging are localized from the same camera images, should ideally not appear at the same time if spatially close to each other. This requires the blinking frequencies of the individual molecular species to be reduced compared with imaging only one color at a time, negating any potential improvement in imaging speed gained by simultaneous multicolor

imaging. Advanced multi-emitter fitting algorithms that simultaneously account for position and spectral identity potentially can remedy this issue in the future.

We achieve low chromatic shifts of 1–5 nm without any chromatic corrections applied in post-processing and independent of how deep we image in a cell. This stands in contrast to the typically 10–20-nm shift between colors when using classical ratiometric approaches, even after applying chromatic corrections in post-processing<sup>16,17</sup>. This advantage is an inherent feature of our SF approach where different dyes are localized from the same camera image using the same spectral detection window. Typical separations between peak emission wavelengths of 20 nm or more thereby are reduced to only 5–9 nm in apparent wavelength difference (Supplementary Fig. 3c–g). To eliminate this spectral shift, an alternative approach is sequentially imaging the same dye by washing out one label and replacing it with a second one between imaging sessions<sup>37,38</sup>. These approaches, however, are only compatible with fixed samples.

While only fixed samples are shown in this work, we would like to emphasize the great potential of the SF approach for live-cell imaging (Supplementary Note 2). A preliminary test using two live-cell-compatible photoactivatable fluorescent dyes, PA-JF646 and PA-JF669, demonstrates that these two dyes can be well separated by the SF approach. Simulations further showed that our approach is compatible with photoactivatable or photoswitchable fluorescent proteins to achieve three-color imaging in live cells with low cross-talk. In concert with other recent developments of live-cell-compatible blinking probes<sup>34</sup>, we believe that our SF approach will be a key to successful multicolor live-cell single-molecule switching microscopy since it eliminates the need for sequential imaging and decreases phototoxicity and photobleaching by using one excitation laser.

## Online content

Any methods, additional references, Nature Research reporting summaries, source data, extended data, supplementary information, acknowledgements, peer review information; details of author contributions and competing interests; and statements of data and code availability are available at <https://doi.org/10.1038/s41592-019-0676-4>.

Received: 1 May 2019; Accepted: 11 November 2019;

Published online: 6 January 2020

## References

1. Ladinsky, M. S., Mastronarde, D. N., McIntosh, J. R., Howell, K. E. & Staehelin, L. A. Golgi structure in three dimensions: functional insights from the normal rat kidney cell. *J. Cell Biol.* **144**, 1135–1149 (1999).
2. Schroeder, L. K. et al. Dynamic nanoscale morphology of the ER surveyed by STED microscopy. *J. Cell Biol.* **218**, 83–96 (2019).
3. Baddeley, D. & Bewersdorf, J. Biological insight from super-resolution microscopy: what we can learn from localization-based images. *Annu. Rev. Biochem.* **87**, 965–989 (2018).
4. Sigal, Y. M., Zhou, R. & Zhuang, X. Visualizing and discovering cellular structures with super-resolution microscopy. *Science* **361**, 880–887 (2018).
5. von Middendorff, C., Egner, A., Geisler, C., Hell, S. W. & Schonle, A. Isotropic 3D nanoscopy based on single emitter switching. *Opt. Express* **16**, 20774–20788 (2008).
6. Shtengel, G. et al. Interferometric fluorescent super-resolution microscopy resolves 3D cellular ultrastructure. *Proc. Natl Acad. Sci. USA* **106**, 3125–3130 (2009).
7. Aquino, D. et al. Two-color nanoscopy of three-dimensional volumes by 4Pi detection of stochastically switched fluorophores. *Nat. Methods* **8**, 353–359 (2011).
8. Huang, F. et al. Ultra-high resolution 3D imaging of whole cells. *Cell* **166**, 1028–1040 (2016).
9. Van Engelenburg, S. B. et al. Distribution of ESCRT machinery at HIV assembly sites reveals virus scaffolding of ESCRT subunits. *Science* **343**, 653–656 (2014).
10. Buttler, C. A. et al. Single molecule fate of HIV-1 envelope reveals late-stage viral lattice incorporation. *Nat. Commun.* **9**, 1861 (2018).
11. Carlini, L., Holden, S. J., Douglass, K. M. & Manley, S. Correction of a depth-dependent lateral distortion in 3D super-resolution imaging. *PLoS One* **10**, e0142949 (2015).
12. Li, Y. M., Wu, Y. L., Hoess, P., Mund, M. & Ries, J. Depth-dependent PSF calibration and aberration correction for 3D single-molecule localization. *Biomed. Opt. Express* **10**, 2708–2718 (2019).
13. Burke, D., Patton, B., Huang, F., Bewersdorf, J. & Booth, M. J. Adaptive optics correction of specimen-induced aberrations in single-molecule switching microscopy. *Optica* **2**, 177–185 (2015).
14. Schonle, A. & Hell, S. W. Fluorescence nanoscopy goes multicolor. *Nat. Biotechnol.* **25**, 1234–1235 (2007).
15. Bossi, M. et al. Multicolor far-field fluorescence nanoscopy through isolated detection of distinct molecular species. *Nano Lett.* **8**, 2463–2468 (2008).
16. Baddeley, D. et al. 4D super-resolution microscopy with conventional fluorophores and single wavelength excitation in optically thick cells and tissues. *PLoS One* **6**, e20645 (2011).
17. Lampe, A., Haucke, V., Sigrist, S. J., Heilemann, M. & Schmoranz, J. Multi-colour direct STORM with red emitting carbocyanines. *Biol. Cell* **104**, 229–237 (2012).
18. Zhang, Z., Kenny, S. J., Hauser, M., Li, W. & Xu, K. Ultrahigh-throughput single-molecule spectroscopy and spectrally resolved super-resolution microscopy. *Nat. Methods* **12**, 935–938 (2015).
19. Mlodzianoski, M. J., Curthoys, N. M., Gunewardene, M. S., Carter, S. & Hess, S. T. Super-resolution imaging of molecular emission spectra and single molecule spectral fluctuations. *PLoS One* **11**, e0147506 (2016).
20. Dempsey, G. T., Vaughan, J. C., Chen, K. H., Bates, M. & Zhuang, X. Evaluation of fluorophores for optimal performance in localization-based super-resolution imaging. *Nat. Methods* **8**, 1027–1036 (2011).
21. Nieuwenhuizen, R. P. et al. Measuring image resolution in optical nanoscopy. *Nat. Methods* **10**, 557–562 (2013).
22. Ries, J., Kaplan, C., Platonova, E., Eghlid, H. & Ewers, H. A simple, versatile method for GFP-based super-resolution microscopy via nanobodies. *Nat. Methods* **9**, 582–584 (2012).
23. Szymborska, A. et al. Nuclear pore scaffold structure analyzed by super-resolution microscopy and particle averaging. *Science* **341**, 655–658 (2013).
24. Schucker, K., Holm, T., Franke, C., Sauer, M. & Benavente, R. Elucidation of synaptosomal complex organization by super-resolution imaging with isotropic resolution. *Proc. Natl Acad. Sci. USA* **112**, 2029–2033 (2015).
25. Schmitt, J. et al. Transmembrane protein Sun2 is involved in tethering mammalian meiotic telomeres to the nuclear envelope. *Proc. Natl Acad. Sci. USA* **104**, 7426–7431 (2007).
26. Barr, F. A., Puype, M., Vandekerckhove, J. & Warren, G. GRASP65, a protein involved in the stacking of Golgi cisternae. *Cell* **91**, 253–262 (1997).
27. Fernandez-Busnadio, R., Saheki, Y. & De Camilli, P. Three-dimensional architecture of extended synaptotagmin-mediated endoplasmic reticulum–plasma membrane contact sites. *Proc. Natl Acad. Sci. USA* **112**, E2004–E2013 (2015).
28. Chung, J. et al. PI4P/phosphatidylserine countertransport at ORP5- and ORP8-mediated ER–plasma membrane contacts. *Science* **349**, 428–432 (2015).
29. Giordano, F. et al. PI(4,5)P<sub>2</sub>-dependent and Ca<sup>2+</sup>-regulated ER–PM interactions mediated by the extended synaptotagmins. *Cell* **153**, 1494–1509 (2013).
30. Li, X. et al. Electron counting and beam-induced motion correction enable near-atomic-resolution single-particle cryo-EM. *Nat. Methods* **10**, 584–590 (2013).
31. Wang, Y. et al. Localization events-based sample drift correction for localization microscopy with redundant cross-correlation algorithm. *Opt. Express* **22**, 15982–15991 (2014).
32. Los, G. V. et al. HaloTag: a novel protein labeling technology for cell imaging and protein analysis. *ACS Chem. Biol.* **3**, 373–382 (2008).
33. Kepller, A. et al. A general method for the covalent labeling of fusion proteins with small molecules in vivo. *Nat. Biotechnol.* **21**, 86–89 (2003).
34. Takakura, H. et al. Long time-lapse nanoscopy with spontaneously blinking membrane probes. *Nat. Biotechnol.* **35**, 773–780 (2017).
35. Douglass, K. M., Sieben, C., Archetti, A., Lambert, A. & Manley, S. Super-resolution imaging of multiple cells by optimised flat-field epi-illumination. *Nat. Photonics* **10**, 705–708 (2016).
36. Deschamps, J., Rowald, A. & Ries, J. Efficient homogeneous illumination and optical sectioning for quantitative single-molecule localization microscopy. *Opt. Express* **24**, 28080–28090 (2016).
37. Pallikkuth, S. et al. Sequential super-resolution imaging using DNA strand displacement. *PLoS One* **13**, e0203291 (2018).
38. Jungmann, R. et al. Multiplexed 3D cellular super-resolution imaging with DNA-PAINT and Exchange-PAINT. *Nat. Methods* **11**, 313–318 (2014).

**Publisher's note** Springer Nature remains neutral with regard to jurisdictional claims in published maps and institutional affiliations.

© The Author(s), under exclusive licence to Springer Nature America, Inc. 2020

## Methods

**Synaptonemal complex samples.** All experimental procedures involving the use of mice were performed in agreement with the Yale University Institutional Animal Care and Use Committee. BALB/c mice were purchased from The Jackson Laboratory (stock no. 000651). Testes (tunica removed) from 18-day-old mice were disrupted using forceps and a razor blade in 1 ml of PBS (1× PBS; Gibco, catalog no. 10010023) with protease inhibitors (Roche, Complete Ultra, catalog no. 05896988001). The cell suspension was then gently added to a 15-ml conical tube with 5 ml of 1× PBS with protease inhibitors and allowed to settle. After approximately 3 min, five 1-ml aliquots of the cell suspension were placed in 1.5-ml microcentrifuge tubes and centrifuged at 9,000 r.p.m. for 10 min. The supernatant was then aspirated, and the pellets were combined in 0.5 ml of 1× Dulbecco's PBS (made from 10× stock; Gibco, catalog no. 14080-055) per testes. Then, 50–100 µl of the cell suspension was added to no. 1.5, 25-mm-diameter round precision coverglass, which had been cleaned and poly-L-lysine coated (Sigma-Aldrich, catalog no. P4707), and allowed to sit for 30 min. The cells on coverglass were then fixed in 4% paraformaldehyde (PFA; Electron Microscopy Sciences, catalog no. 15710) for 15 min at room temperature. Standard immunolabeling was performed using the antibodies listed in the “Synaptonemal complex labeling” section.

**Cell culture.** COS-7 and HeLa cells were grown in DMEM or DMEM/F12 (Gibco, catalog nos. 21063029 and 21041025) supplemented with 10% fetal bovine serum (Gibco, catalog no. 10438026) at 37°C with 5% CO<sub>2</sub>. Some cultures were grown with media supplemented with sodium pyruvate (Gibco, catalog no. 11360070).

**Plasmids.** For labeling the ER membrane, we expressed the plasmid mEmerald-Sec61-C-18, a gift from Michael Davidson (deceased, formerly Florida State University, Tallahassee, FL, USA; Addgene plasmid no. 54249), which encodes GFP-Sec61β. For labeling mitochondria, we expressed GFP-OMP25 from a plasmid that was made by modifying pEGFP-C1 (Takara Bio) to have eGFP fused to the C terminus of human OMP25/SYNJ2BP complementary DNA containing the amino acids ‘QVQNGPIGHRGEGDPSGIPIFMVLVPVFALTIVAAWFMRYRQQL’ and that localizes to mitochondria, as shown previously<sup>39</sup>. For labeling the medial Golgi, we expressed GFP-ManII from a plasmid that was made from pEGFP-N1 (Takara Bio) to have amino acids 1–137 of mouse Man2a1 fused to GFP, such that GFP is located in the Golgi lumen. For labeling the ER lumen, we expressed mCherry-KDEL from a plasmid that was made by modifying pDsRed2-ER (Takara Bio), which encodes a signal peptide fused to DsRed2, followed by the tetrapeptide ER retention signal KDEL. The mCherry gene was amplified using the following primers: 5'-ATACCGGTGATGGTGAGCAAGGGCGAG-3' and 5'-CTGAAGCTTTACAGCTCGCTCTTGTACAGCTCGTCCATGCC-3'. The pDsRed2-ER plasmid and the mCherry PCR product were both digested using AgeI and HindIII (New England Biolabs, catalog nos. R0552S and R3104S) and ligated together, replacing the DsRed2 gene with the mCherry gene. Plasmids encoding GFP-ORP5 and mCherry-ORP5 were previously published<sup>38</sup>. Plasmids encoding mCherry-E-Syt2 and GFP-E-Syt2 were also previously published<sup>29</sup>.

**Coverglass cleaning.** Precision-thickness coverglass (Bioscience Tools, catalog no. CSHP-No1.5-25) was cleaned before cells were plated on it. Before plating COS-7 cells, glass was cleaned in a sonic bath (Bronson) immersed in 1 M KOH for 15 min and then rinsed with Milli-Q water three times. Glass was then sterilized with 100% ethanol, incubated with poly-L-lysine for 10 min, then rinsed with sterile PBS before adding media and cells. Before plating HeLa cells, glass was instead cleaned with an ozone cleaner (Jelight, UVO Cleaner, catalog no. 342A) for 30 min. Media and HeLa cells were placed directly on ozone-cleaned glass. Before placing spermatocytes, glass was cleaned in a plasma oven for 5 min before being coated with poly-L-lysine.

**Transfection.** Samples including GFP-Sec61β, mCherry-KDEL and GFP-OMP25 expression in HeLa or COS-7 cells used DNA transfection by electroporation. DNA was introduced to HeLa or COS-7 cells using a NEPA GENE electroporation device. Approximately 1 million cells were rinsed in Opti-MEM (Gibco, catalog no. 31985070) and then resuspended in Opti-MEM with 10 µg of DNA in an electroporation cuvette with 2-mm gap (Bulldog Bio, catalog no. 12358346). Cells were electroporated with a poring pulse of 125 V, 3-ms pulse length, 50-ms pulse interval, 2 pulses, with decay rate of 10% and +polarity; followed by a transfer pulse of 25 V, 50-ms pulse length, 50-ms pulse interval, 5 pulses, with a decay rate of 40% and ±polarity. After electroporation, the cells were removed from the cuvette and grown in growth medium on prepared coverglass (see Coverglass cleaning section). Samples were fixed 18–24 h after electroporation.

Samples including ER-PM contact site protein expression in COS-7 cells utilized Lipofectamine2000 (Invitrogen, catalog no. 11668027) transfection. The day before transfection, cells were plated on prepared coverglass. Transfection was performed as suggested by the manufacturer with a modification of 1 µl of transfection reagent and 1 µg of DNA per well in a six-well plate. When two DNAs were transformed together, 0.5 µg of each DNA was used for a total of 1 µg of DNA. We did not find that different transfection approaches affected the image quality.

**Fluorescent dyes.** Alexa Fluor 647 (AF647) and CF660C were used for all two-color imaging experiments, except for the ER-PM imaging where CF680 was

used instead of CF660C (see ER-PM contact sites labeling section). Secondary antibodies labeled with AF647 (Invitrogen, catalog no. A21236, A21237 or A21245; used at 1:1,000 dilution for 1 h at room temperature) and CF660C (Biotium, catalog no. 20812-500 µl or 20813-500 µl; used at 1:500 or 1:1,000 dilution for 1 h at room temperature) were used to label primary antibodies. These CF660C-labeled antibodies were manufactured to have one dye per antibody. Nanobody GFP-binding protein (Chromotek, catalog no. gt-250) and RFP-binding protein (Chromotek, catalog no. rt-250) were conjugated to AF647 in the laboratory (see Nanobody and antibody conjugation section).

Dyomics 634 (DY634), DyLight 650 (DL650) and CF680 were used for all three-color imaging experiments. Secondary antibodies labeled with DY634 (conjugated in the laboratory, see Nanobody and antibody conjugation section; used at 1:200 dilution for 1 h at room temperature), DL650 (Invitrogen, catalog no. SA5-10174 or SA5-10034; used at 1:1,000 dilution for 1 h at room temperature) and CF680 (Biotium, catalog no. 20817-500 µl or 20818-500 µl; used at 1:500 or 1:1,000 dilution for 1 h at room temperature) were used to label primary antibodies. The CF680-labeled antibodies were manufactured to have one dye per antibody. Nanobody RFP-binding protein conjugated to DY634 and nanobody GFP-binding protein conjugated to DL650 were made in the laboratory (see Nanobody and antibody conjugation section). WGA-CF680 (Biotium, catalog no. 29029-1) was used for PM labeling.

**Nanobody and antibody conjugation.** Nanobody RFP-binding protein or GFP-binding protein was conjugated to Alexa Fluor 647 NHS-ester (Life Technologies, catalog no. A20006), DY634 NHS-ester (Dyomics, catalog no. DY-634-NHS-ester portionized, 634-01A) or DL650 NHS-ester (Thermo Scientific, catalog no. 62265). Approximately 100-µl conjugations were performed in 0.1 M sodium bicarbonate for 1 h in the dark. Excess dye was removed from the conjugation reaction using Zeba Spin Desalting Columns with a 7 kDa molecular weight cut off (Thermo Scientific, catalog no. 89882). Nanobodies were used at 1:1,000 dilution at room temperature or overnight at 4°C.

Unlabeled goat anti-rabbit IgG, goat anti-mouse IgG and goat anti-human IgG (Jackson ImmunoResearch, catalog nos. 111-005-144, 115-005-146 and 109-005-088, respectively) were conjugated with DY634 NHS-ester (Dyomics, DY-634-NHS-ester portionized, 634-01A). Approximately 100-µl reactions were performed in 0.1 M sodium bicarbonate for 1 h in the dark. Excess dye was removed from antibody using Pro-Spin columns (Princeton Separations, catalog no. CS800) per manufacturer's recommendations. Secondary antibodies conjugated in this work were used at 1:200 for 1 h at room temperature.

**Sample labeling. Microtubule samples.** To label microtubules, COS-7 cells were prepared as previously reported<sup>8</sup>. After growing on poly-L-lysine-coated coverglass for 24 h, cells were rinsed with PBS, warmed to 37°C, then incubated for 1 min in 0.05% saponin diluted in cytoskeletal buffer (CBS; 10 mM MES pH 6.1, 138 mM NaCl, 3 mM MgCl<sub>2</sub>, 2 mM EGTA, 320 mM sucrose), warmed to 37°C. Cells were subsequently fixed in 3% PFA and 0.1% glutaraldehyde (GA; Electron Microscopy Sciences, catalog no. 16019) diluted in CBS, warmed to 37°C. Cells were permeabilized and blocked with 3% BSA (Jackson ImmunoResearch, catalog no. 001-000-162) and 0.2% Triton X-100 (TX-100; Sigma-Aldrich, catalog no. T8787) in 1× PBS (diluted from 10× PBS; American Bio, catalog no. AB11072-0100) for 30 min. The samples were incubated overnight at 4°C with mouse anti-α-tubulin antibody (Sigma-Aldrich, catalog no. T5168) diluted to 1:200 in antibody dilution buffer (1% BSA and 0.2% TX-100 in 1× PBS). Cells were washed in wash buffer (0.05% TX-100 in 1× PBS) three times for 5 min each. For single-color labeling, microtubule samples were incubated with each dye-conjugated secondary antibody (used at 1:1,000) in antibody dilution buffer for 1 h at room temperature then washed three times for 5 min with wash buffer. For two- or three-color labeling, microtubule samples were incubated with the dye-conjugated secondary antibodies (used at 1:1,000) together. Lastly, the samples were post-fixed in 3% PFA + 0.1% GA in CBS for 10 min, rinsed with PBS three times and stored in PBS at 4°C until imaged.

**ER and microtubule labeling.** COS-7 cells overexpressing GFP-Sec61β and were grown on poly-L-lysine-coated glass for 24 h before being fixed with 3% PFA + 0.1% GA in PBS for 15 min at room temperature. Samples were rinsed three times in 1× PBS before permeabilizing for 3 min using permeabilization buffer (0.3% CA-630 (Sigma-Aldrich, catalog no. I8896), 0.05% TX-100, 0.1% BSA and 1× PBS) at room temperature. Samples were then rinsed three times with 1× PBS followed by 1 h in blocking buffer (0.05% CA-630, 0.05% TX-100, 5% normal goat serum (Jackson ImmunoResearch, catalog no. 005-000-121) and 1× PBS). Primary antibodies: rabbit anti-GFP (Invitrogen, catalog no. A11122, used at 1:500) and mouse anti-tubulin (used at 1:1,000), were diluted in blocking buffer and incubated with samples overnight at 4°C. Samples were then washed in wash buffer (0.05% CA-630, 0.05% TX-100, 0.2% BSA and 1× PBS) three times for 5 min each before secondary antibody labeling for 1 h at room temperature diluted in blocking buffer. Samples were washed in wash buffer three times for 5 min each. Post-fixation was performed using 3% PFA + 0.1% GA in 1× PBS for 10 min. Samples were rinsed three times in 1× PBS before being stored in 1× PBS at 4°C.

**ER membrane and ER lumen labeling.** COS-7 cells overexpressing GFP-Sec61β alone or GFP-Sec61β and mCherry-KDEL together were plated on cleaned and

poly-L-lysine-coated glass and grown for 24 h before being fixed in 3% PFA + 0.1% GA in 1× PBS for 15 min.

All ER samples were permeabilized with permeabilization buffer (0.3% CA-630, 0.05% TX-100, 0.1% BSA and 1× PBS) for 3 min at room temperature, rinsed in 1× PBS three times and then blocked in blocking buffer (0.05% CA-630, 0.05% TX-100, 5% normal goat serum and 1× PBS) for 1 h. Samples were washed in wash buffer (0.05% CA-630, 0.05% TX-100, 0.2% BSA and 1× PBS) three times for 5 min each after labeling with primary antibody, secondary antibody or nanobody. The ER was labeled using different combinations of antibodies and/or nanobodies.

For two-color ER membrane labeling with antibodies, GFP-Sec61 $\beta$  was labeled with rabbit anti-GFP which was then labeled with two competing secondary antibodies. For two-color ER membrane labeling combining nanobody and antibody, GFP-binding protein nanobody, conjugated with AF647, first was used to label GFP-Sec61 $\beta$  at room temperature for 1 or 2 h. Then, rabbit anti-GFP (used at 1:500) was incubated with samples at 4°C overnight. The samples were subsequently labeled with a secondary antibody conjugated to CF660C. Two-color ER membrane and lumen labeling was performed on cells expressing GFP-Sec61 $\beta$  and mCherry-KDEL. Lumen-localized mCherry-KDEL was first labeled using RFP-binding protein nanobody conjugated to AF647 for 2 h at room temperature. GFP-Sec61 $\beta$  was then labeled using rabbit anti-GFP (used at 1:500 at 4°C overnight) which was then labeled with CF660C. All samples were post-fixed using 3% PFA + 0.1% GA in 1× PBS for 10 min. Samples were rinsed three times in 1× PBS before being stored in 1× PBS at 4°C.

**Mitochondria labeling.** HeLa cells were used for imaging mitochondria. For some samples, GFP-OMP25 was overexpressed for 18–24 h. Mitochondria samples were fixed differently depending on the primary antibody being used, with a preference for 3% PFA + 0.1% GA in 1× PBS for 15 min at room temperature. Samples that included mouse anti-dsDNA antibody labeling, since this primary antibody does not label cells if GA is used during fixation, were fixed using 4% PFA in 1× PBS for 1 h at room temperature. All cells were permeabilized with permeabilization buffer (0.3% CA-630, 0.05% TX-100, 0.1% BSA and 1× PBS) for 3 min at room temperature, rinsed three times in PBS and then blocked in blocking buffer (0.05% CA-630, 0.05% TX-100, 5% normal goat serum and 1× PBS).

Primary antibodies were diluted in blocking buffer and incubated with samples according to the antibody used. For outer mitochondria/outer mitochondria two-color samples, mouse anti-GFP (Invitrogen, catalog no. A11120, used at 1:500) was incubated on samples at 4°C overnight followed by rabbit anti-TOM20 (Abcam, catalog no. ab78547, used at 1:1,000) on samples at room temperature for 1 h. For outer mitochondria/nucleoid two-color samples, mouse anti-dsDNA (Abcam, catalog no. ab27156, used at 1:1,000) was incubated with samples at 4°C overnight followed by rabbit anti-TOM20 (used at 1:500) on samples at room temperature for 1 h the following day. When labeling inner and outer mitochondria, the inner mitochondria primary and secondary labeling was completed before beginning labeling the outer mitochondria. After each antibody labeling, samples were washed in wash buffer (0.05% CA-630, 0.05% TX-100, 0.2% BSA and 1× PBS) three times for 5 min. Two-color samples were labeled with AF647 and CF660C secondary antibodies. Post-fixation was performed using 3% PFA + 0.1% GA in PBS for 10 min. Samples were rinsed three times in PBS before being stored in PBS at 4°C.

**Synaptonemal complex labeling.** After being fixed with 4% PFA, the samples were then washed with 1× PBS three times followed by a permeabilization step using 0.5% TX-100 in 1× PBS for 10 min at room temperature. Samples were then rinsed in 0.1% TX-100 in PBS and treated with Image-iT Signal Enhancer (Molecular Probes, catalog no. I36933) for 30 min at room temperature. After three washes in 0.1% TX-100 in PBS, the samples were incubated in blocking buffer (0.05% TX-100, 5% normal goat serum, 0.05%, in 1× PBS) for 30 min at room temperature. For SYCP3 and SYCP1-C (or SYCP1-N) two-color samples, rabbit anti-SYCP1-C (Novus Biologicals, catalog no. N300-229, used at 1:500) (or rabbit anti-SYCP1-N (ref. <sup>24</sup>), a gift from Dr. Ricardo Benavente of University of Wuerzburg, used at 1:500) was incubated with samples at 4°C overnight followed by mouse anti-SYCP3 (Abcam, catalog no. ab97672, used at 1:500) on samples at room temperature for 1 h the following day. After each primary antibody labeling, samples were washed in wash buffer (0.05% CA-630, 0.05% TX-100, 0.2% BSA and 1× PBS) three times for 5 min. Two-color samples were labeled with AF647 and CF660C secondary antibodies. For SYCP3/SYCP1-C/Lamin B three-color samples, rabbit anti-SYCP1-C (used at 1:500) was incubated with samples at 4°C overnight. The next day, mouse anti-SYCP3 (used at 1:500) was incubated with samples at room temperature for 1 h followed by a 1-h incubation at room temperature with chicken anti-Lamin B (Abcam, catalog no. ab90169, used at 1:200). After each primary antibody labeling, samples were washed in wash buffer (0.05% CA-630, 0.05% TX-100, 0.2% BSA and 1× PBS) three times for 5 min. Three-color samples were labeled with CF680 (used at 1:1,000), DY650 (used at 1:1,000) and Dyomics 634 (used at 1:200) secondary antibodies. For synaptonemal complex samples, we performed the imaging when they were freshly made and avoided the extra washing steps associated with post-fixation that may remove cells from the sample. On entry into meiosis, the nuclear lamina is disrupted, leading to the fragmented appearance shown in Fig. 2 and Supplementary Video 4.

**Golgi labeling.** Since we did not identify a good anti-ManII antibody suitable for immunolabeling, we electroporated HeLa cells with a plasmid encoding ManII-GFP to label the medial Golgi apparatus. Cells were transferred to cleaned coverglass and the plasmid expressed for 18–24 h, before being fixed with 4% PFA in 1× PBS for 15 min at room temperature. Cells were permeabilized with permeabilization buffer (0.3% CA-630, 0.05% TX-100, 0.1% BSA and 1× PBS) for 3 min at room temperature, rinsed three times in PBS and then blocked in blocking buffer (0.05% CA-630, 0.05% TX-100, 5% normal goat serum and 1× PBS).

Primary antibodies were diluted in blocking buffer and incubated with samples according to the antibodies used. For *cis*/medial/*trans*-labeled samples, mouse anti-p230 (BD Bioscience, catalog no. 611280, used at 1:1,000) and nanobody GFP-binding protein, conjugated with DL650, were incubated with samples at 4°C overnight followed by rabbit anti-GRASP65 (Abcam, catalog no. ab174834, used at 1:2,000) on samples for 1 h at room temperature the next day. Alternatively, for *cis/cis*/medial-labeled samples, mouse anti-GM130 (BD Bioscience, catalog no. 610822, used at 1:500) and nanobody GFP-binding protein, conjugated with DL650, were incubated on samples together at 4°C overnight followed by rabbit anti-GRASP65 (used at 1:3,000) on samples for 1 h at room temperature the next day. After each antibody labeling, samples were washed in wash buffer (0.05% CA-630, 0.05% TX-100, 0.2% BSA and 1× PBS) three times for 5 min. After labeling with both primary antibodies and nanobody, samples were incubated with secondary antibodies labeled with DY634 and CF680 together. Samples were post-fixed using 3% PFA + 0.1% GA in PBS for 10 min. Samples were rinsed three times in PBS before being stored in PBS at 4°C.

**ER–PM contact sites labeling.** COS-7 cells were grown on poly-L-lysine-coated glass and transfected with plasmids encoding the following proteins: GFP-Sec61 $\beta$ , GFP-ORP5, mCherry-ORP5, GFP-E-Syt2 or mCherry-E-Syt2 (in different combinations) using Lipofectamine2000. Cells were fixed with 3% PFA + 0.1% GA 18–24 h after transfection. If the PM was lectin-labeled, the samples were labeled directly after fixation but before permeabilization. Cells were rinsed with Hanks' balanced salt solution (HBSS; Gibco, catalog no. 14025-092) three times before labeling with 1  $\mu$ g ml<sup>-1</sup> WGA-CF680 (Biotium, 29029-1) diluted in HBSS for 10–30 min at room temperature. Cells were then rinsed three times in HBSS and once in PBS before being permeabilized using permeabilization buffer (0.3% CA-630, 0.05% TX-100, 0.1% BSA and 1× PBS) for 3 min at room temperature. Samples were rinsed three times in PBS and blocked for at least 1 h with blocking buffer (0.05% CA-630, 0.05% TX-100, 5% normal goat serum and 1× PBS). Primary antibodies and/or nanobodies in blocking buffer were incubated with samples overnight at 4°C.

For two-color samples labeling ER and PM (expressing GFP-Sec61 $\beta$ ) and two-color samples labeling contact proteins and PM (expressing GFP-ORP5 or GFP-E-Syt2), GFP was labeled with rabbit anti-GFP (used at 1:500 overnight at 4°C) followed by a secondary AF647 antibody. Some ER and PM samples also expressed mCherry-ORP5 or mCherry-E-Syt2, which were not immunolabeled. For two-color samples labeling ER and contact proteins (expressing GFP-Sec61 $\beta$  with either mCherry-ORP5 or mCherry-E-Syt2), rabbit anti-mCherry (Abcam, catalog no. ab167453 used at 1:500 or 1:1,000 overnight at 4°C) and mouse anti-GFP (used at 1:500 overnight at 4°C) were used to label the fluorescent proteins, followed by secondary antibodies labeled with AF647 and CF660C. For three-color samples labeling ER, contact site proteins and PM (expressing GFP-Sec61 $\beta$  with either mCherry-ORP5 or mCherry-E-Syt2), WGA was used to label the PM, and rabbit anti-mCherry (used at 1:500 or 1:1,000 overnight at 4°C) and mouse anti-GFP (used at 1:500 overnight at 4°C) were used to label the fluorescent proteins, followed by secondary antibodies labeled with DY634 and DL650. Post-fixation was performed using 3% PFA + 0.1% GA in PBS for 10 min. Samples were rinsed three times in PBS before being stored in PBS at 4°C.

**Mitochondria and microtubules.** COS-7 cells were used for two-color labeling of mitochondria and microtubules. Cells were grown on cleaned and poly-L-lysine-coated glass before being fixed in 3% PFA + 0.1% GA in 1× PBS for 15 min. Samples were rinsed three times in PBS before permeabilizing for 3 min using permeabilization buffer (0.3% CA-630, 0.05% TX-100, 0.1% BSA and 1× PBS) at room temperature. Samples were then rinsed three more times with PBS followed by 1 h in blocking buffer (0.05% CA-630, 0.05% TX-100, 5% normal goat serum and 1× PBS). Primary antibodies rabbit anti-TOM20 (used at 1:500) and mouse anti-tubulin (used at 1:1,000) were diluted in blocking buffer and incubated with samples overnight at 4°C. Samples were then washed in wash buffer (0.05% CA-630, 0.05% TX-100, 0.2% BSA and 1× PBS) three times for 5 min each before secondary antibody labeling for 1 h at room temperature diluted in blocking buffer. Samples were then washed in wash buffer three times for 5 min each. Post-fixation was performed using 3% PFA + 0.1% GA in PBS for 10 min. Samples were rinsed three times in PBS before being stored in PBS at 4°C.

**Imaging buffer and sample mounting.** The conventional β-mercaptoethanol (βME) STORM imaging buffer was prepared as previously reported<sup>40</sup>. The imaging buffer was made every time immediately before use, where catalase and glucose oxidase were diluted in base buffer (50 mM Tris pH 8.0, 50 mM NaCl, 10% glucose) with the addition of βME (Sigma-Aldrich, catalog no. M3148-25ML). The final

concentration of  $\beta$ ME was 143 mM. The samples were mounted in a custom-designed sample holder as previously described<sup>8</sup>. Briefly, the sample coverslip was mounted in the sample holder facing up. Then, 100  $\mu$ l of imaging buffer was evenly spread on the sample coverslip and a clean coverslip was put on top (attention was given to avoid bubbles being trapped between the two coverslips). Excess imaging buffer was drained using Kimwipes. The samples were then sealed with two-component silicone glue (Picodent Twinsil, Picodent). After the silicone glue had hardened (typically 20–30 min), the samples were transferred to the 4Pi-SMS microscope for imaging. The imaging buffer would usually allow for about 8–10 h of imaging.

**Multicolor 4Pi-SMS setup.** The multicolor 4Pi-SMS system was built based on the previously described instrument<sup>8</sup> with minor modifications (Supplementary Fig. 1). The oil immersion objectives were replaced with high-numerical-aperture silicone immersion objectives ( $\times 100/1.35$  numerical aperture, Olympus) for better refractive index matching. The system was equipped with two excitation lasers at 560 nm (MPB Communications, 2RU-VFL-P-2000-560-B1R) and 642 nm (MPB Communications, 2RU-VFL-2000-642-B1R), and an activation laser at 405 nm (Coherent OBIS 405 LX, 50 mW). Details about the dichroic beamsplitter and emission filters used in the system are shown in Supplementary Fig. 1b. The conventional fluorescence follows the same emission path as the previous design and is collected by an scientific complementary metal-oxide-semiconductor (sCMOS) camera (ORCA-Flash 4.0v2, Hamamatsu) (Supplementary Fig. 1a, Camera 1). The SF is reflected by the dichroic beamsplitter to the back side of the system and collected by an electron-multiplying charge-coupled device (EMCCD) camera (128  $\times$  128 pixels, iXon DU860, Andor) (Supplementary Fig. 1c, Camera 2). Both cameras were controlled by custom-written LabVIEW (National Instruments) programs.

**Image acquisition.** During image acquisition, the sCMOS camera was set to external trigger mode and the EMCCD camera was set to internal trigger and frame transfer mode. For synchronization, the Fire output of the EMCCD camera was used to trigger the sCMOS camera. The electron multiplication gain of the EMCCD camera was set to 200 for all experiments. Biological samples were imaged at 100 Hz with a laser (642 nm) intensity of about 7.5 kW cm<sup>-2</sup> (two-color imaging) or 200 Hz at about 15 kW cm<sup>-2</sup> (three-color imaging). The 405-nm activation laser was manually adjusted to maintain a low density of single molecules per frame. For samples thicker than 1  $\mu$ m, the stage was translated at 500-nm steps every 3,000 frames for multiple times to cover the entire volume. Typically, 180,000–360,000 frames were recorded, which corresponds to acquisition times of 15 min to 1 h.

**Image analysis and color assignment.** The images recorded with the sCMOS camera (conventional fluorescence) were analyzed as previously described<sup>8</sup>. Briefly, the lateral positions ( $x$ ,  $y$ ) of single molecules were determined by fitting with sCMOS-specific algorithms<sup>40</sup>. The phase values ( $z$  positions) were estimated from the 0th moment Gaussian intensities of the four images and unwrapped using the metric developed previously<sup>8</sup>. To translate the phase values to axial positions, the intensity modulation frequency for each dye was determined from the simulated 4Pi point spread functions using a pupil function-based approach<sup>41</sup>. The simulation was performed using the average wavelength of the detected emission spectra in the conventional fluorescence channel of each dye (Supplementary Fig. 3c–g). For the images recorded with the EMCCD camera (SF), the readout counts were converted to photoelectrons using the conversion factor provided by the manufacturer. Then, the pixel-wise median operation (time window = 3,000 frames) in MATLAB (MathWorks) was used as a filter algorithm to remove the background signals. The positions of localized molecules in the sCMOS images were then mapped to the EMCCD images using a second-order affine transformation matrix obtained by imaging a fluorescent bead sample. The corresponding regions in the EMCCD images were cropped out (5  $\times$  5 pixels, 170-nm pixel size) and multiplied by a normalized two-dimensional (2D) Gaussian distribution with a standard deviation of 130 nm centered at the positions of the molecules. This Gaussian weighting was performed to reduce the influence from the background regions. The intensity of the molecules in the EMCCD images was calculated by summing the values of the Gaussian-weighted regions. For color assignment, the intensities of the molecules in the SF and conventional fluorescence images were plotted on a logarithmic scale (Fig. 1d,h) and binned to a 2D histogram intensity image (Supplementary Figs. 4g and 5j). An appropriate threshold (typically 2% of each peak value) was applied to separate the different dye molecules with a low cross-talk (Supplementary Figs. 4g,h and 5j,k). After color assignment, the phase-unwrapped values of the dye molecules from the sCMOS images were translated to axial positions using the wavelength-dependent modulation frequencies obtained above. Localizations ( $x$ ,  $y$  and  $z$ ) from all color channels were combined for drift correction using a custom algorithm based on redundant cross-correlation<sup>30,31,42</sup>. We performed two iterations, the first round with linear interpolation in each time window followed by a second round without interpolation. The residual drift in each direction is typically less than 5 nm after correction. For samples requiring axial stepping, multiple optical sections were aligned using a 3D cross-correlation method<sup>30</sup>. Localizations that appeared in consecutive frames within a radius of two times the localization precision

were considered to represent the same molecule and were combined. Localized molecules were rejected based on the following criteria: photon number < 500, lateral localization precision > 25 nm, interference contrast < 0.4 or log-likelihood ratio > 300. Particularly, we found the log-likelihood ratio<sup>43</sup> to be a very effective metric to reduce multi-emitter artifacts. All 4Pi-SMS images and videos were rendered with Vutara SRX software (Bruker). Briefly, the intensity-based images were rendered using Point Splatting mode (10–30-nm particle size), which represents each molecule as a 3D Gaussian distribution with a full-width at half-maximum (FWHM) of the same size. For the overview images, the pixel size is 4–8 nm. For the enlarged regions, the pixel size is 2–4 nm.

**Thickness and separation measurements of the Golgi cisternae.** For each 3D Golgi volume, we cropped 1- $\mu$ m-wide subregions along the  $x$  or  $y$  direction. We manually reoriented the subregions to generate 2D projection images providing a side view of the region of the Golgi stack to be analyzed (Fig. 3f,g and Supplementary Fig. 10e,f). Next, we took line profiles (thickness = 100 nm) at positions where the three markers were parallel to each other (Fig. 3f and Supplementary Fig. 10f). Each intensity profile was fit by a Gaussian function to determine the thickness (estimated as the FWHM of the Gaussian distribution when applicable) and the separation between cisternae (distance between peak positions).

**Quantification of the ER-PM contact sites images.** The two-color images of the contact site proteins (ORP5 or E-Syt2) and PM (Supplementary Fig. 11b,c) were automatically divided into  $100 \times 100$ -nm<sup>2</sup>  $x$ - $y$  subregions. To ensure a high signal-to-noise ratio, only subregions with more than 100 localizations from the PM labeling (WGA) and 300 localizations from ORP5 (or E-Syt2) were kept for further data analysis (more than 2,800 subregions for each condition). The WGA labeling featured much brighter staining of the top PM compared with the bottom PM, which resulted in much higher WGA localization densities at the top PM than the bottom PM. We therefore used the top PM signal only for distance measurements. WGA localizations with  $z$  positions below the median  $z$  positions of ORP5 (or E-Syt2) were rejected as they were considered to belong to the bottom PM. The remaining  $z$  positions of WGA and the  $z$  positions of ORP5 (or E-Syt2) were binned into histograms (with 5-nm bin size), respectively. The histograms of WGA and ORP5 (or E-Syt2) localizations were both fit by Gaussian functions to determine the two peak positions and the distance between them (Fig. 4g). In Fig. 4d,f,i,k, the line plots were generated from the corresponding rendered images. Localizations were binned at a pixel size of 3–4 nm (slightly varying depending on the field-of-view) and Gaussian-blurred with a standard deviation of 4.2 nm (FWHM = 10 nm).

**Simulation of the SF approach performance.** The SF signal is mainly determined by the transition wavelength of the dichroic beamsplitter while the conventional fluorescence signal is determined by the spectral window confined by the dichroic beamsplitter and the emission filter (in front of Camera 1, Supplementary Fig. 1a). The performance of the SF approach is therefore expected to depend on the choice of the transition wavelength of the dichroic beamsplitter. To investigate this phenomenon, we performed simulations for transition wavelengths ranging from 650 nm to 680 nm (Supplementary Fig. 2). To use realistic simulation parameters, we based our simulation on experimental data. For each dye, we randomly selected 2 million single molecules from real imaging experiments. The photon number of each molecule (determined from the conventional fluorescence channel) was converted to the total photon number representing the whole emission spectrum, taking the experimentally used spectral detection window into account. Next, we took the transition profile of a commercially available dichroic beamsplitter (Semrock Di01-R405/488/561/635) that features a steep rising edge in the ~657-nm range. The transition wavelength of the dichroic beamsplitter was defined as the wavelength at which the transmission is 50%. The transmission profile starts to rise at 650 nm. Below that value, we assumed 2% transmission. Above 664 nm, we assumed 98% transmission. For our simulation, we shifted this transition profile across the spectrum starting at a transition wavelength of 650 nm and ending at 680 nm, with the assumption that the conventional fluorescence channel collects the transmitted signal up to 750 nm and the SF channel collects the reflected signal upwards from 645 nm (based on the used excitation laser wavelength of 642 nm). The fraction of conventional fluorescence and SF was calculated for each simulation and photon numbers were allocated to each channel accordingly. We then generated synthetic single-molecule images based on these photon numbers in each channel and added background and readout noise similar to experimentally observed values. Finally, these images were analyzed in the same way as experimental data, and the cross-talk and localization precisions were calculated taking advantage of the ground truth provided by the simulation and averaged for 2 million simulated molecules each.

We found that less than 10% of Alexa 647 (when compared with CF660C) and DL650 (when compared with CF680) molecules were rejected at transition wavelengths of 661 nm or above, and 662 nm or above, respectively. As expected, localization precision degraded with increasing transition wavelengths, since larger transition wavelengths lead to narrower conventional fluorescence spectral windows. Up to 670-nm transition wavelength, the loss in localization precision

stayed below 2 nm, which we considered acceptable. The dichroic beamsplitter used in our microscope (Chroma ZT405/488/561/647rpc) features a transition wavelength of 668 nm, which falls within this acceptable window between 661 nm or 662 nm on the lower end and 670 nm on the upper end.

Although we selected commercially available dichroic beamsplitters and emission filters in this work, it is possible to increase the collection efficiency of the conventional fluorescence channel by using custom dichroic beamsplitters with a transition edge closer to the excitation wavelength. For dual-objective systems, collecting SF at both objectives can further improve the performance. Additionally, the detected SF can be used to improve the localization precision but at the cost of image registration error and added complexity in the data analysis.

**Statistics.** The average separation between GM130 and GRASP65 (Fig. 3*i*) was determined to be not significantly different from zero ( $P=0.62$ ) by using a two-tailed Student's *t*-test in MATLAB.

**Reporting Summary.** Further information on research design is available in the Nature Research Reporting Summary linked to this article.

## Data availability

The datasets generated and/or analyzed during the current study, technical drawings and parts lists are available from the corresponding author upon reasonable request. Source data for Figs. 1 and 3 are provided with the paper.

## Code availability

Custom MATLAB code about the color assignment for the salvaged fluorescence approach used during the current study is available at: <https://github.com/bewersdorflab/salvaged-fluorescence>.

## References

39. Nemoto, Y. & De Camilli, P. Recruitment of an alternatively spliced form of synaptosomal protein 2 to mitochondria by the interaction with the PDZ domain of a mitochondrial outer membrane protein. *EMBO J.* **18**, 2991–3006 (1999).
40. Huang, F. et al. Video-rate nanoscopy using sCMOS camera-specific single-molecule localization algorithms. *Nat. Methods* **10**, 653–658 (2013).
41. Hanser, B. M., Gustafsson, M. G., Agard, D. A. & Sedat, J. W. Phase-retrieved pupil functions in wide-field fluorescence microscopy. *J. Microsc.* **216**, 32–48 (2004).
42. Hoess, P., Mund, M., Reitberger, M. & Ries, J. Dual-color and 3D super-resolution microscopy of multi-protein assemblies. *Methods Mol. Biol.* **1764**, 237–251 (2018).
43. Huang, F., Schwartz, S. L., Byars, J. M. & Lidke, K. A. Simultaneous multiple-emitter fitting for single molecule super-resolution imaging. *Biomed. Opt. Express* **2**, 1377–1393 (2011).

## Acknowledgements

We thank R. Benavente (University of Wuerzburg) for sharing the anti-SYCP1-N antibody, A. E. S. Barentine and A. M. Ernst (Yale University) for comments on the manuscript and C. G. Ebeling (Bruker Corp.) for help with the Vutara SRX software. This work was primarily supported by grants from the Wellcome Trust (grant no. 203285/B/16/Z), the G. Harold and Leila Y. Mathers Foundation and the NIH (grant nos. R01 GM118486, P30 DK045735 and NS36251). Y.L. acknowledges support from the EMBL Interdisciplinary Postdoc Programme (EIPOD) under Marie Curie Actions COFUND. J.B.G. and L.D.L. were funded by the Howard Hughes Medical Institute.

## Author contributions

Y.Z. and J.B. conceived the idea. Y.Z. implemented the hardware. Y.Z., Y.L., J.R. and D.B. wrote the software. L.K.S., J.C., P.D.C., J.E.R. and J.B. designed biological experiments. L.K.S. developed sample preparation protocols. L.K.S. prepared and optimized microtubule, ER, mitochondria, Golgi and ER-PM contact sites samples. Y.S. and L.B. provided the synaptosomal complex samples. M.D.L. prepared and optimized the synaptosomal complex samples. P.K. prepared and optimized microtubule samples. Y.Z. imaged the samples and analyzed the images. J.B.G. and L.D.L. synthesized PA-JF646 and PA-JF669. Y.Z., L.K.S. and J.B. wrote the manuscript with input from all authors. All authors discussed the results and commented on the manuscript.

## Competing interests

J.B. has financial interests in Bruker Corp. and Hamamatsu Photonics. J.B. is co-inventor of a US patent application (US20170251191A1) related to the 4Pi-SMS system and image analysis used in this work. Y.Z. and J.B. have filed a US patent application about the salvaged fluorescence multicolor imaging method described in this work.

## Additional information

**Supplementary information** is available for this paper at <https://doi.org/10.1038/s41592-019-0676-4>.

**Correspondence and requests for materials** should be addressed to J.B.

**Peer review information** Rita Strack was the primary editor on this article and managed its editorial process and peer review in collaboration with the rest of the editorial team.

**Reprints and permissions information** is available at [www.nature.com/reprints](http://www.nature.com/reprints).

Corresponding author(s): Joerg Bewersdorff

Last updated by author(s): Oct 29, 2019

## Reporting Summary

Nature Research wishes to improve the reproducibility of the work that we publish. This form provides structure for consistency and transparency in reporting. For further information on Nature Research policies, see [Authors & Referees](#) and the [Editorial Policy Checklist](#).

### Statistics

For all statistical analyses, confirm that the following items are present in the figure legend, table legend, main text, or Methods section.

n/a Confirmed

- The exact sample size ( $n$ ) for each experimental group/condition, given as a discrete number and unit of measurement
- A statement on whether measurements were taken from distinct samples or whether the same sample was measured repeatedly
- The statistical test(s) used AND whether they are one- or two-sided  
*Only common tests should be described solely by name; describe more complex techniques in the Methods section.*
- A description of all covariates tested
- A description of any assumptions or corrections, such as tests of normality and adjustment for multiple comparisons
- A full description of the statistical parameters including central tendency (e.g. means) or other basic estimates (e.g. regression coefficient) AND variation (e.g. standard deviation) or associated estimates of uncertainty (e.g. confidence intervals)
- For null hypothesis testing, the test statistic (e.g.  $F$ ,  $t$ ,  $r$ ) with confidence intervals, effect sizes, degrees of freedom and  $P$  value noted  
*Give  $P$  values as exact values whenever suitable.*
- For Bayesian analysis, information on the choice of priors and Markov chain Monte Carlo settings
- For hierarchical and complex designs, identification of the appropriate level for tests and full reporting of outcomes
- Estimates of effect sizes (e.g. Cohen's  $d$ , Pearson's  $r$ ), indicating how they were calculated

*Our web collection on [statistics for biologists](#) contains articles on many of the points above.*

### Software and code

Policy information about [availability of computer code](#)

Data collection

Data collection was performed using custom code written in LabVIEW 2012 (National Instruments). The program is available from the corresponding author upon request.

Data analysis

Data analysis was performed using custom code written in MATLAB 2017b (MathWorks). Custom code about the color assignment for the salvaged fluorescence approach used during the current study is available at <https://github.com/bewersdorflab/salvaged-fluorescence>. Vutara SRX 6.04.07 (Bruker) was used for 3D visualization. ImageJ 1.50c and ImageJ (Fiji) 1.8.0\_172 was used to crop images, generate line profiles and similar tasks.

For manuscripts utilizing custom algorithms or software that are central to the research but not yet described in published literature, software must be made available to editors/reviewers. We strongly encourage code deposition in a community repository (e.g. GitHub). See the Nature Research [guidelines for submitting code & software](#) for further information.

### Data

Policy information about [availability of data](#)

All manuscripts must include a [data availability statement](#). This statement should provide the following information, where applicable:

- Accession codes, unique identifiers, or web links for publicly available datasets
- A list of figures that have associated raw data
- A description of any restrictions on data availability

The datasets generated and/or analyzed during the current study are available from the corresponding author on request. An example dataset can be downloaded from <https://www.dropbox.com/sh/qw18jf3qcma1pbj/AACVAfhZ0WxM87vW-5Vgrvlaa?dl=0>

# Field-specific reporting

Please select the one below that is the best fit for your research. If you are not sure, read the appropriate sections before making your selection.

- Life sciences       Behavioural & social sciences       Ecological, evolutionary & environmental sciences

For a reference copy of the document with all sections, see [nature.com/documents/nr-reporting-summary-flat.pdf](http://nature.com/documents/nr-reporting-summary-flat.pdf)

## Life sciences study design

All studies must disclose on these points even when the disclosure is negative.

|                 |   |
|-----------------|---|
| Sample size     | This is a methods paper describing a technological development. No sample size calculation was performed. Our sample size was selected to adequately demonstrate the technical performance of our instrument.   |
| Data exclusions | Qualitative exclusion criteria for accepting or rejecting imaged samples were pre-established based on comparisons to previously published images and preliminary experiments performed during the optimization process of the method development. Localized molecules were rejected based on the following criteria: photon number < 500, lateral localization precision > 25 nm, interference contrast < 0.4 or log-likelihood ratio > 300. |
| Replication     | All attempts at replication were successful. The exact number of independent experiments are provided in the figure legends.  |
| Randomization   | No randomization was performed. Randomization was considered to be not necessary as the purpose of the study was to demonstrate a new technique and not report biological results.  |
| Blinding        | No blinding was performed. Blinding was considered to be not necessary as the purpose of the study was to demonstrate a new technique and not report biological results.  |

## Reporting for specific materials, systems and methods

We require information from authors about some types of materials, experimental systems and methods used in many studies. Here, indicate whether each material, system or method listed is relevant to your study. If you are not sure if a list item applies to your research, read the appropriate section before selecting a response.

| Materials & experimental systems    |   | Methods                             |   |
|-------------------------------------|---|-------------------------------------|---|
| n/a                                 | Involved in the study   | n/a                                 | Involved in the study                           |
| <input type="checkbox"/>            | <input checked="" type="checkbox"/> Antibodies                  | <input checked="" type="checkbox"/> | <input type="checkbox"/> ChIP-seq               |
| <input type="checkbox"/>            | <input checked="" type="checkbox"/> Eukaryotic cell lines       | <input checked="" type="checkbox"/> | <input type="checkbox"/> Flow cytometry         |
| <input checked="" type="checkbox"/> | <input type="checkbox"/> Palaeontology                          | <input checked="" type="checkbox"/> | <input type="checkbox"/> MRI-based neuroimaging |
| <input type="checkbox"/>            | <input checked="" type="checkbox"/> Animals and other organisms |                                     |   |
| <input checked="" type="checkbox"/> | <input type="checkbox"/> Human research participants            |                                     |   |
| <input checked="" type="checkbox"/> | <input type="checkbox"/> Clinical data                          |                                     |   |

## Antibodies

### Antibodies used

Commercial primary antibodies:  
 mouse anti- $\alpha$ -tubulin antibody (Sigma-Aldrich, Cat# T5168, used at 1:200 or 1:1000)  
 rabbit anti-GFP (Invitrogen, Cat# A11122, used at 1:500)  
 mouse anti-GFP (Invitrogen, Cat# A11120, used at 1:500)  
 rabbit anti-TOM20 (Abcam, Cat# ab78547, used at 1:500 or 1:1000)  
 mouse anti-dsDNA (Abcam, Cat# ab27156, used at 1:1000)  
 rabbit anti-SYCP1-C (Novus Biologicals, Cat# N300-229, used at 1:500)  
 rabbit anti-SYCP1-N (A gift from Dr. Ricardo Benavente, used at 1:500)  
 mouse anti-SYCP3 (Abcam, Cat# ab97672, used at 1:500)  
 chicken anti-LaminB (Abcam, Cat# ab90169, used at 1:200)  
 mouse anti-p230 (BD Bioscience, Cat# 611280, used at 1:1000)  
 rabbit anti-GRASP65 (Abcam, Cat# ab174834, used at 1:2000 or 1:3000)  
 mouse anti-GM130 (BD Bioscience, Cat# 610822, used at 1:500)  
 rabbit anti-mCherry (Abcam, Cat# ab167453 used at 1:500 or 1:1000)

Commercial dye-conjugated secondary antibodies:  
 Goat anti-Mouse-AF647 IgG (H+L) (Invitrogen, Cat# A21236, used at 1:1000)  
 F(ab')2-Goat anti-Mouse-AF647 IgG (H+L) (Invitrogen, Cat# A21237, used at 1:1000)  
 Goat anti-Rabbit-AF647 IgG (H+L) (Invitrogen, Cat# A21245, used at 1:1000)  
 Goat anti-Mouse-CF660C-ST IgG (H+L) (Biotium, Cat# 20812-500 $\mu$ L, used at 1:500 or 1:1000)

Goat anti-Rabbit-CF660C-ST IgG (H+L) (Biotium, Cat# 20813-500µL, used at 1:500 or 1:1000)  
 Goat anti-Mouse-DL650 IgG (H+L) (Invitrogen, Cat# SA5-10174, used at 1:1000)  
 Goat anti-Rabbit-DL650 IgG (H+L) (Invitrogen, Cat# SA5-10034, used at 1:1000)  
 Goat anti-Mouse-CF680-ST IgG (H+L) (Biotium, Cat# 20817-500µL, used at 1:500 or 1:1000)  
 Goat anti-Rabbit-CF680-ST IgG (H+L) (Biotium, Cat# 20818-500µL, used at 1:500 or 1:1000)

Commercial unconjugated antibodies/nanobodies:  
 Nanobody GFP-binding protein (Chromotek, Cat# gt-250)  
 Nanodboy RFP-binding protein (Chromotek, Cat# rt-250)  
 goat anti-rabbit IgG (Jackson ImmunoResearch, Cat# 111-005-144)  
 goat anti-mouse IgG (Jackson ImmunoResearch, Cat# 115-005-146)  
 goat anti-human IgG (Jackson ImmunoResearch, Cat# 109-005-088)

## Validation

The results of all commercial antibodies are consistent with the information shown on respective manufacturers' websites, where many references are listed. Below we list one reference for each antibody.

mouse anti- $\alpha$ -tubulin antibody - DOI: 10.1083/jcb.104.2.289  
 rabbit anti-GFP - DOI: 10.1371/journal.pone.0197899  
 mouse anti-GFP - DOI: 10.1038/s41467-018-07307-6  
 rabbit anti-TOM20 - DOI: 10.1016/j.biopha.2018.10.123  
 mouse anti-dsDNA - DOI: 10.1093/nar/gky1305  
 rabbit anti-SYCP1-C - DOI: 10.1371/journal.pone.0209995  
 rabbit anti-SYCP1-N - DOI: 10.1073/pnas.1414814112  
 mouse anti-SYCP3 - DOI: 10.7554/elife.39304  
 chicken anti-LaminB - DOI: 10.1155/2019/2750528  
 mouse anti-p230 - DOI: 10.1074/jbc.271.14.8328  
 rabbit anti-GRASP65 - DOI: 10.3390/biom8040150  
 mouse anti-GM130 - DOI: 10.1083/jcb.200205115  
 rabbit anti-mCherry - DOI: 10.1016/j.molmet.2018.11.005  
 Goat anti-Mouse-AF647 IgG (H+L) - DOI: 10.1016/j.ntt.2016.10.004  
 F(ab')2-Goat anti-Mouse-AF647 IgG (H+L) - DOI: 10.1038/nature22047  
 Goat anti-Rabbit-AF647 IgG (H+L) - DOI: 10.3389/fnana.2016.00124  
 Goat anti-Mouse-CF660C-ST IgG (H+L) - DOI: 10.1038/nmeth.3528  
 Goat anti-Rabbit-CF660C-ST IgG (H+L) - DOI: 10.1038/nmeth.3528  
 Goat anti-Mouse-DL650 IgG (H+L) - DOI: 10.1089/neu.2019.6509  
 Goat anti-Rabbit-DL650 IgG (H+L) - DOI: 10.1016/j.chembiol.2018.06.009  
 Goat anti-Mouse-CF680-ST IgG (H+L) - DOI: 10.1038/nmeth.3528  
 Goat anti-Rabbit-CF680-ST IgG (H+L) - DOI: 10.1038/nmeth.3528  
 Nanobody GFP-binding protein - DOI: 10.1038/nmeth.4605  
 Nanodboy RFP-binding protein - DOI: 10.1126/science.aaa5619  
 goat anti-rabbit IgG - DOI: 10.3892/etm.2018.6942  
 goat anti-mouse IgG - DOI: 10.1242/jeb.191106  
 goat anti-human IgG - DOI: 10.1177/1087057115609564

All self-conjugated nanobodies/secondary antibodies are validated in this work.

## Eukaryotic cell lines

Policy information about [cell lines](#)

|  |   |
|--|---|
| Cell line source(s)  | COS-7 ATCC batch #63624240, HeLa ATCC CCL-2   |
| Authentication   | Cell lines were freshly purchased from ATCC directly and not independently authenticated. |
| Mycoplasma contamination   | Cell lines were not tested for mycoplasma contamination.                                  |
| Commonly misidentified lines<br>(See <a href="#">ICLAC</a> register) | No ICLAC cell lines were used.  |

## Animals and other organisms

Policy information about [studies involving animals; ARRIVE guidelines](#) recommended for reporting animal research

|                         |   |
|-------------------------|---|
| Laboratory animals      | Male 18-day old BALB/CJ mice (The Jackson Laboratory, Stock No: 000651) were used.  |
| Wild animals            | The study did not involve wild animals.   |
| Field-collected samples | The study did not involve samples collected from the field.   |
| Ethics oversight        | All experimental procedures involving the use of mice were performed in agreement with the Yale University Institutional Animal Care and Use Committee (IACUC). |

Note that full information on the approval of the study protocol must also be provided in the manuscript.